NANO LETTERS

Letter

pubs.acs.org/NanoLett

Crossed Ga_2O_3/SnO_2 Multiwire Architecture: A Local Structure Study with Nanometer Resolution

Gema Martínez-Criado,*[,†] Jaime Segura-Ruiz,[†] Manh-Hung Chu,[†] Remi Tucoulou,[†] Iñaki López,[‡] Emilio Nogales,[‡] Bianchi Mendez,[‡] and Javier Piqueras[‡]

[†]European Synchrotron Radiation Facility, 38043-Grenoble, France

[‡]Departamento de Física de Materiales, Facultad de Ciencias Físicas, Universidad Complutense de Madrid, 28040-Madrid, Spain

Supporting Information

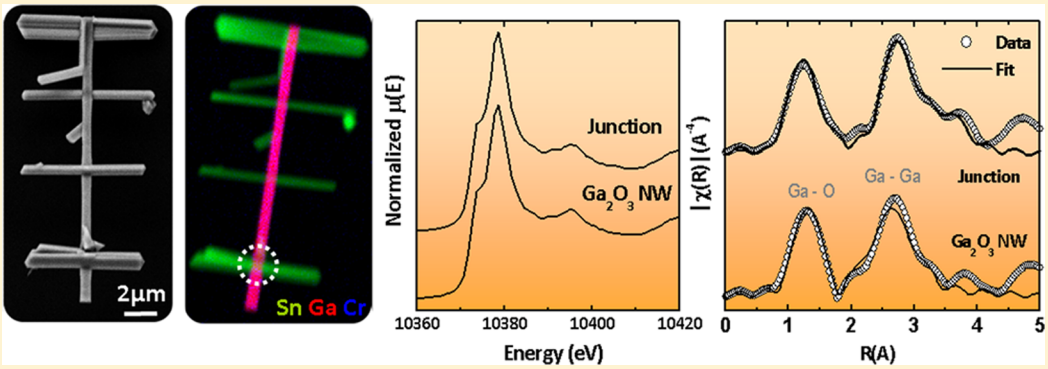

ABSTRACT: Crossed nanowire structures are the basis for high-density integration of a variety of nanodevices. Owing to the critical role of nanowires intersections in creating hybrid architectures, it has become a challenge to investigate the local structure in crossing points in metal oxide nanowires. Thus, if intentionally grown crossed nanowires are well-patterned, an ideal model to study the junction is formed. By combining electron and synchrotron beam nanoprobes, we show here experimental evidence of the role of impurities in the coupling formation, structural modifications, and atomic site configuration based on crossed Ga_2O_3/SnO_2 nanowires. Our experiment opens new avenues for further local structure studies with both nanometer resolution and elemental sensitivity.

KEYWORDS: *Crossed nanowires, local structure, X-ray nanoprobe, X-ray fluorescence, nanodevices*

Nanowires have been proposed as an ideal system for the assembly of a wide range of applications such as memory, sensing, logic, light emission and waveguide. Large-scale integration of nanowires into functional circuits will require practical interconnections for nanoscale devices. In this context, substantial attention has been paid to develop crossed semiconducting nanowires.[1] By assembling crossed nanowires into junctions, an integrated FET and light-emitting diode (LED) has been created by Lieber et al.[2] So far, the quality of the nanowire junctions has been mostly gauged by electrical transport and optical techniques.[3,4] Additionally, indirect methods such as scanning electrochemical cell microscopy,[5] inelastic electron tunneling,[6] and Raman scattering[7] have been also used to determine local heterogeneous electron transfer kinetics and cooperative effects in a two-dimensional network of nanowires. However, the formation of such individual components also needs a systematic structural and chemical study of point contacts between different nanowires.

Although the selection of structural phases during growth is a key step in the development of nanowires for nanodevice applications, so far there are many open challenges; just few examples include the role of impurities on coupling formation and local atomic site configuration, how single nanowires are joined to form multiwires, whether there is a full control over composition, diffusion paths, and/or structural modifications, the coexistence of zinc-blende and wurtzite structures in diffusion-driven growth,[8,9] phase separation problems,[10] mobility degradation by the presence of stacking faults,[11] strong diameter dependence of the crystal structure,[12] size-dependent defect density,[13] radial modulation doping,[14] as well as atomic scale variability due to fluctuations in the growth rate.[15] Techniques such as transmission electron microscopy and powder X-ray diffraction (XRD) have yielded information about these issues. However, in many cases the atomic structural rearrangements are still unexplored. Powder X-ray diffraction has been used to model the structure of ensembles of nanowires, and it is possible to obtain fits of XRD patterns by assuming bulk lattice parameters. But, the information content in XRD patterns is limited, particularly with respect to aperiodic

Received: February 28, 2014
Revised: August 24, 2014

   dx.doi.org/10.1021/nl502156h | *Nano Lett.* XXXX, XXX, XXX−XXX

parts of single nanowires (e.g., crossing points or nanowire junctions).

Consequently, apart from a few cases in which single crystal X-ray diffraction patterns of nanowires could be recorded,[10,16] almost no information about the symmetry of individual nanowires and their intersections is available. A technique with the potential to measure structural disorder including atomic configurations is X-ray absorption spectroscopy. The cross section of an absorbing atom depends on the scattering of the generated photoelectron wave from neighboring atoms, thereby including information about the local structure around the absorber. Because of the local nature, this process does not rely on any long-range order in a sample. Also, extended X-ray absorption fine structure (EXAFS) has proven to be a valuable tool to investigate doping induced changes in nanowires.[10] Whereas EXAFS mainly probes the radial arrangement of neighboring atoms with respect to the absorbing atom, the spectrum within 50 eV above the absorption edge, X-ray absorption near-edge structure (XANES) is sensitive to the relative arrangement of multiple atoms due to the increased contribution of multiple-scattering effects. Nevertheless, most of the local up-to-date structural analyses on nanowires have reported average interatomic distances over a macroscopic volume.[17,18] If nanofocusing optics is added to an X-ray absorption experiment, the challenge of study single nanowires can be overcome using X-ray nanobeams.

Recently, a couple of reports have published the first application of nano-X-ray absorption spectroscopy to single nanowires.[10,19] Here we extend the use of an X-ray nanobeam to the study of a junction created during the growth of multiwires. Our focus on the intersection of such a nanocross is motivated not only by the observed morphological changes,[20−22] and/or elemental diffusion,[23−25] but also by the important local recrystallization and consequent atomic reorganization that could take place at the crossing points of the wires.[26−28] Depending on the merging angle between two nanowires, a mixture of structural phases, grain boundary defects, or a single-crystalline structure at the junctions[29−31] have been reported. The impact of the structural changes of the wire junctions on the transport properties is very critical. The formation of defect complexes or phase separation that changes the local structure has a strong connection with a lower conductivity and mobility at the nanojunctions. Moreover, not only are the transport properties affected but some contact areas could be optically unavailable because of the unwanted structural changes. As a consequence, the intersections may result in increased electrical scattering regions between segments due to an induced structural instability, which imposes an obstacle for realization of basic multiple arm blocks for future nanoscale devices.

Earlier efforts have led to demonstration of nanowire-based FETs and basic devices configured using a crossed nanowire geometry, including p−n diodes and bipolar transistors.[32,33] However, the electrical properties of nanowires in these proof-of-concept studies were far from optimal, leading to low apparent carrier mobilities and large sample to sample variations. Recently, for example, InSb nanowires with controlled structural properties have enabled the formation of nanowire crosses designed to explore potential configurations for Majorana Fermion exchange.[31] Therefore, here we address such issues by characterizing a nanowire junction formed by Ga-doped SnO_2 nanowires that lie across one Cr-doped Ga_2O_3 nanowire obtained in a one-step thermal evaporation method based on a vapor−solid (VS) mechanism. Five polymorphs of Ga_2O_3 (α, β, γ, δ, and ε) have been reported so far, but only two phases (α and β) are well-known structures. In particular, the β-Ga_2O_3 with monoclinic structure is the thermodynamically stable phase, which consists of tetrahedral GaO_4 and octahedral GaO_6 units in a 1:1 ratio, whereas Ga atoms in α-Ga_2O_3 (trigonal structure) are only in octahedral coordination. The phase transition from β-Ga_2O_3 to α-Ga_2O_3 has been reported under high-pressure conditions.[34] Finally, the spinel γ-Ga_2O_3 also possess both tetrahedral and octahedral cation sites but with different ratios in comparison with the β-Ga_2O_3. On the other hand, the stable phase of SnO_2 is the rutile structure, in which Sn occupies octahedral sites in the crystalline lattice. It is important to emphasize that the wire junctions considered in the present work result from growth phenomena and not from laying wires across one another.

In addition, the incorporation of dopant impurities during the growth process may locally alter the crystalline phases of involved oxides at the wires junctions, because impurities might be located at available tetrahedral or octahedral coordinated sites in the host lattice. Thus, in this work we have carried out the study of wires' junctions by synchrotron X-ray fluorescence imaging, X-ray absorption spectroscopy, and scanning electron microscopy techniques with nanometer spatial resolution. These techniques are capable of monitoring nearest neighbors atomic distances and symmetry of the local environment just at the crossing points. Because Ga_2O_3 usually behaves as a n-type semiconductor and Ga doped SnO_2 exhibits p-type conductivity, the contact region would end in a p−n nanojunction, which is a basic building block for the fabrication of nanodevices. Therefore, based on their high surface to volume ratios and small active sizes, gallium oxide and tin oxide nanowires are potential wide-band gap materials for optoelectronics and sensor nanodevices. In addition, because the crossed multiwire system results from a self-organization mechanism, a single-step evaporation-deposition process could be enough to achieve p−n nanojunctions (there is no need of postgrowth manipulation of individual wires to interconnect them).

Under an inert atmosphere and using pure elements as material sources, the one-step synthesis is based on a vapor−solid (VS) growth of metal oxide nanowires on substrates of the same oxide. So far, this deposition method has been used to obtain nanowires of Ga_2O_3, GeO_2, or SbO_2 from pure Ga, Ge, or Sb, respectively.[35−37] Compared to vapor−liquid−solid (VLS) process, which usually requires gold nanoparticles to drive the nanowire growth, this procedure is catalyst free. However, the doping has proven to be elusive in metal oxide nanostructures because of the out-diffusion processes that usually led to rather low impurity concentration. In this context, there is still a lack of fundamental understanding of the mechanisms involved to get effectively doped nanostructures.[38,39] Moreover, it has been observed that the presence of dopant in the precursor modifies the morphology of the synthesized nanostructures. For example, indium oxide addition to the Ga precursor led to the formation of Ga_2O_3 nanobelts with stepped surfaces caused by In segregation during the crystal growth.[20] Alternatively, the presence of tin oxide has been found to play a major role in the lateral growth of branches from wires due to a catalytic effect at the surfaces of the nanowires.[40] In both cases, high-resolution transmission electron microscopy (HRTEM) techniques have shown a

dx.doi.org/10.1021/nl502156h | Nano Lett. XXXX, XXX, XXX−XXX

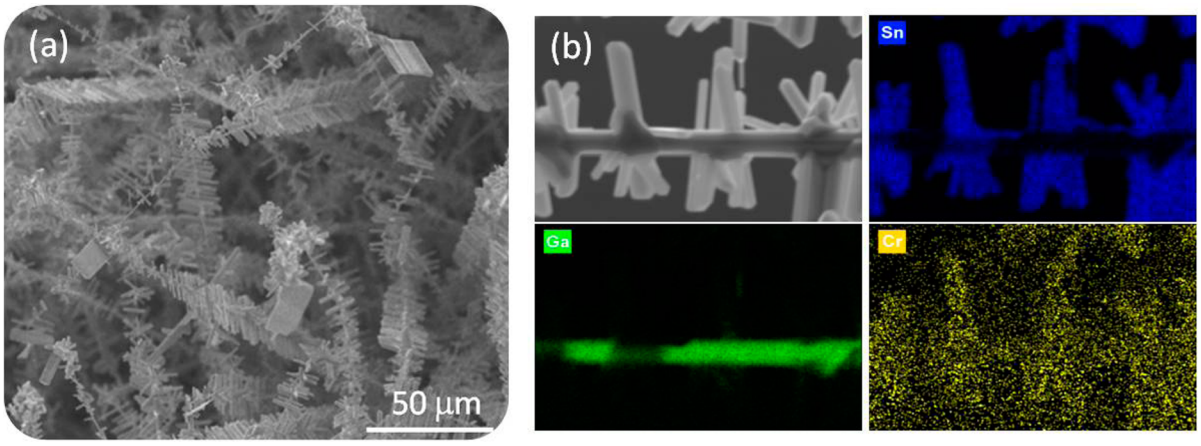

Figure 1. (a) SEM image of branched nanostructures grown on the gallium oxide pellet. (b) SEM image and EDS mapping for Sn, Ga, and Cr of an isolated structure on a silicon wafer.

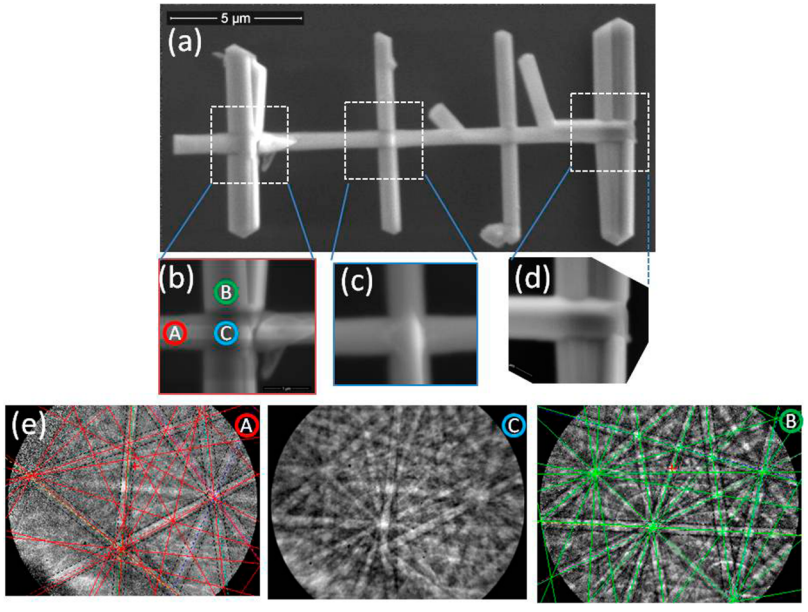

Figure 2. (a) SEM image of a selected branched nanostructures grown on the gallium oxide pellet. (b–d) Details of the crossing points. (e) Kikuchi patterns from points **A**, **B**, and **C** labeled in (b). Point **A** corresponds to the trunk, point **B** is representative for branches, and point **C** is the intersection between trunk and branches. Kikuchi lines were indexed according to the monoclinic Ga_2O_3 in **A** and the rutile SnO_2 phase in **B**. Lines at point **C** are a mixed combination of both phases.

monoclinic (β-Ga_2O_3) crystalline phase for doped Ga_2O_3 micro- and nanowires.

In this work, crossed Ga_2O_3/SnO_2 multiwire architectures were grown by thermal evaporation from metallic gallium placed on a gallium oxide pellet with both tin oxide and chromium oxide powders on its surface. We focused on Sn and Cr doping because Sn induces the nucleation of branches in Ga_2O_3 nanowires, while Cr ions produce strongly luminescent centers in Ga_2O_3 host with potential optical applications.[41] The samples were thermally treated for 16 h at 1500 °C under an argon flux of 0.8 L per minute. Figure 1a shows a general view of the structures grown on the gallium oxide pellet, which mostly consisted of long branched wires. The structures were dispersed onto a silicon wafer to perform their characterization using both X-ray and electron beam probes.

In Figure 1b, energy dispersive X-ray spectroscopy (EDS) by scanning electron microscopy (SEM) shows that Sn is located only in the branches, while Ga is confined mainly in the trunk axis. In the SnO_2 branches Ga doping is also present at trace levels. This architecture, consisting of trunk and lateral branches, is reproducible over many structures. In good agreement, representative electron back scattered diffraction (EBSD) patterns (Figure 2) reveal a main Cr doped Ga_2O_3 nanowire (600 nm diameter and 18 μm length) crossed perpendicularly by several SnO_2 nanowires (~600 nm diameter and 7 μm length). The EBSD measurements highlight that the crystalline structure of the lateral branches is the rutile phase of SnO_2, while Kikuchi patterns from the trunk are indexed as the monoclinic phase of β-Ga_2O_3. Figure 2b displays the detail of one of the crossing regions, where labels A, B, and C stands for trunk, branch, and junction, respectively. Kikuchi lines were indexed according to the monoclinic β-Ga_2O_3 phase in **A** and the rutile SnO_2 phase in **B**, whereas Kikuchi pattern from point **C** is a mixed combination of both phases (Figure 2e). A series of nine EBSD patterns recorded along a line from the SnO_2 branch to the Ga_2O_3 wire passing through the intersection area

dx.doi.org/10.1021/nl502156h | *Nano Lett.* XXXX, XXX, XXX–XXX

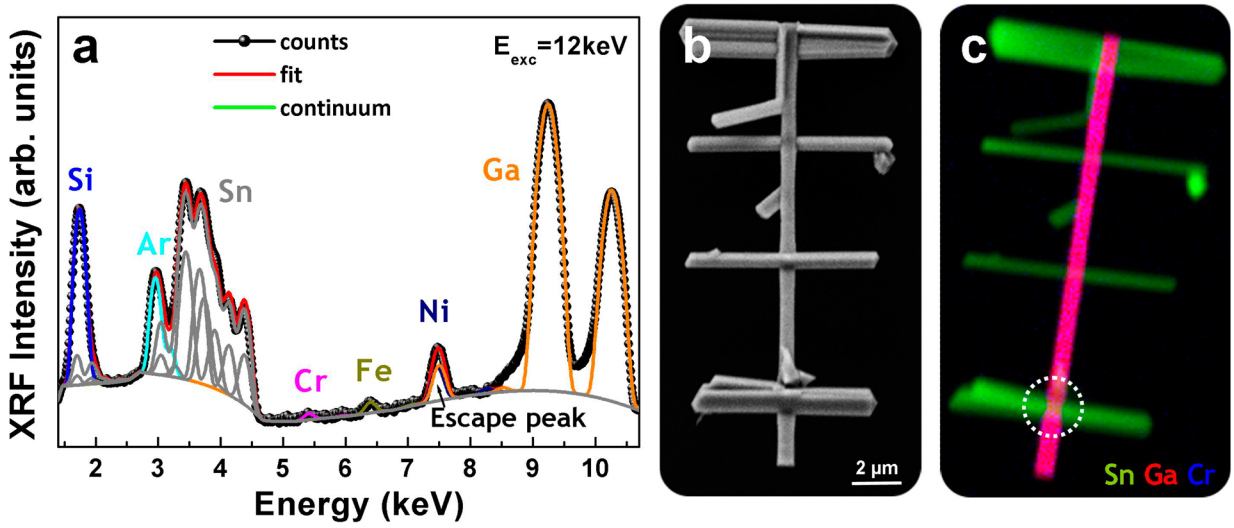

Figure 3. (a) Average XRF spectrum recorded over a 12 × 20 μm^2 area of the crossed multiwire structure shown in Figure 2a at 12 keV. (b) Scanning electron microscopy image of the structure. (c) XRF map in RGB visualization that depicts the XRF intensities of Sn (green), Ga (red), and Cr (blue). Their color brightness (light represents high counts, dark low counts) indicates the intensity ranges. Map size: 12 × 20 μm^2; pixel size: 100 nm; counting time: 0.5 s/point. The highlighted region is magnified in Figure 4.

is provided in the Supporting Information Figure S1. The images show a smooth transition from rutile-SnO_2 to Ga_2O_3 phases: lines corresponding to crystallographic planes in rutile are fading, while new sets of lines of monoclinic β-Ga_2O_3 arise.

A more accurate chemical composition analysis was performed with the use of a hard X-ray nanoprobe at the undulator beamline ID22 at the European Synchrotron Radiation Facility (ESRF).[42] The goal was to probe compositional heterogeneities and local symmetry within the single crossed multiwire SnO_2/Ga_2O_3 structures. Using a pair of Kirkpatrick-Baez Si mirrors, the experimental approach involved the collection of X-ray fluorescence (XRF) emissions induced by a highly focused and intense hard X-ray monochromatic beam [100 × 100 nm^2 spot size ($V \times H$) with 5 × 10^{10} ph/s at 12 keV] at room temperature in air environment. The emission of characteristic secondary X-rays was recorded with an energy dispersive Si drift detector located at $\theta = (15 \pm 5)°$ with respect to the sample surface. The spatial resolution of the experimental arrangement is governed by the spot size of the incident X-ray beam and the excitation volume. In combination with the high brightness of the third-generation synchrotron source, the diffraction limited X-ray lenses allowed for nanoscale lateral and chemical analysis with short acquisition times (typically from 200 ms to 1 s per spectrum).[43]

Figure 3 shows the X-ray nanoimaging results obtained by scanning over a 12 × 20 μm^2 area of the single multiwire structure shown in Figure 2a. Figure 3a displays the average XRF of the probed area, while Figure 3b (SEM image) shows the geometry of the structure with a SnO_2 nanowire spacing of about 5 μm along the Ga_2O_3 nanowire axial direction. With regular separations and similar sizes and shapes, as expected at the length scale of the beam size, the XRF map of the crossed multiwire structure exhibits clearly high contrast between Sn and Ga major elements, as well as for Cr, dopant element present in the Ga_2O_3 wire (Figure 3c). There are small features associated with the morphological heterogeneities observed by SEM. The highlighted region (dashed circle), which corresponds to the location where EBSD measurements were acquired (Figure 2), is magnified in Figure 4. The X-ray fluorescence measurements identify the precise spatial location

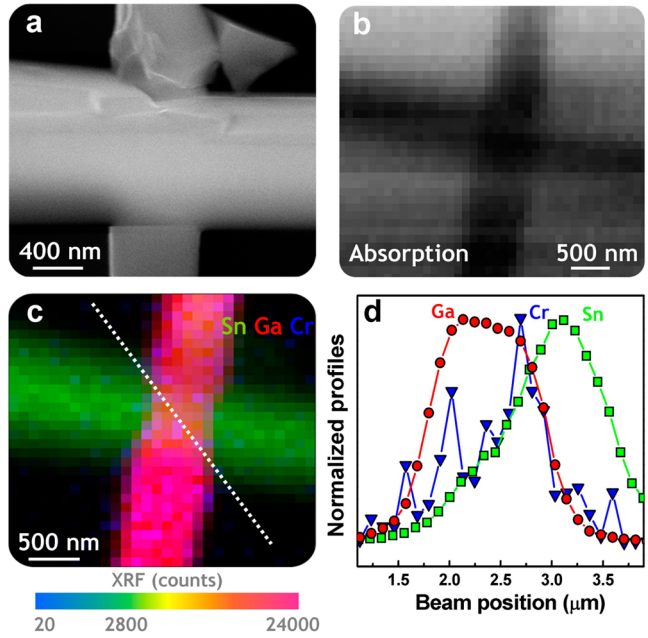

Figure 4. (a) Scanning electron microscopy image of the nanowire junction. (b) X-ray transmission image of the intersection region obtained at 12 keV. (c) Magnified view of the highlighted area of the XRF map in RGB visualization. (d) Normalized XRF line profiles for Sn (green symbols), Ga (red symbols), and Cr (blue symbols), respectively, collected along the white dotted line shown in (a).

of the crossing point and reveal that, according to the targeted architecture, the distribution of the major elements follows the expected pattern for the crossed multiwire array (Figure 3c). The average XRF spectrum exhibits, besides Ar and Si from the air and Si substrate respectively, peaklike structures statistically significant and attributed to unintentional Fe and Ni elemental traces.

Apart from the X-ray transmission image (Figure 4b) of the area shown in the SEM image of Figure 4a, Figure 4d shows the relative intensities of the Ga, Sn, and Cr characteristic lines normalized to the maximum peak height, which have been

dx.doi.org/10.1021/nl502156h | Nano Lett. XXXX, XXX, XXX−XXX

collected along the white dotted line shown in Figure 4c. As expected, within the sensitivity of our experimental setup both Cr and Ga elements show a close correlation on their spatial locations that are nearly colocalized. Although the measurements could suffer from the effects of shadowing and sample aspect ratio alignment with respect to the detector, along the points of the scanned line, the monotonous changes in the elemental profiles suggest no remarkable interdiffusion along the junction. The estimation of the concentration of the dopants Ga in SnO_2 (Cr and Sn in Ga_2O_3) wires has been performed using PyMca code.[44] The resulting values are about (0.72 ± 0.01) atom % Ga in SnO_2 $[(6.07 \pm 0.01)$ atom % Sn and (0.014 ± 0.004) atom % Cr in $Ga_2O_3]$. It has been reported that the occurrence of interdiffusion via formation of mixed spinel structures at heterointerfaces plays a crucial role on the resulting physical properties like, for example, the magnetic response.[23,24] Here, the XRF findings point to a rather uniform crossed multiwire structure, without relevant signatures of junction-induced defects, elemental diffusion, and/or agglomeration effects. The connection between the dopant incorporation and structural information is discussed further on.

In order to get deeper insight into the local structure of the crossing point, the gallium partial density of states in the conduction band has been probed inside and outside the nanowire junction using nano-X-ray absorption spectroscopy. The XANES measurements were performed with a Si(111) double crystal monochromator at room temperature. The energy resolution under these conditions was estimated to be approximately 1 eV. Figure 5 depicts the spatially resolved XANES data recorded in XRF detection mode at the Ga K-edge. In general, Ga_2O_3 has five polymorphs (α, β, γ, δ, and ε) but only two phases have well-known structures (α and β), because of the poor crystallinity of other gallium oxides. β-Ga_2O_3 with monoclinic structure is the thermodynamically stable phase, whereas ε-Ga_2O_3 presents the lowest symmetry. Compared to the β-Ga_2O_3, spinel γ-Ga_2O_3 also possess both tetrahedral and octahedral cation sites but with different ratios. Figure 5a shows the XANES spectra of three reference compounds with different Ga environments. In GaAs, Ga atoms are in regular tetrahedral sites, whereas in α-Ga_2O_3 Ga atoms are in distorted octahedral sites. Finally, Ga atoms present mixed coordination composed by equal GaO_4 and GaO_6 units in β-Ga_2O_3. Thus, following the dipolar selection rules, the XANES spectra exhibit a prominent white line mainly assigned to 1s $\rightarrow$ 4p dipole transitions, while postedge resonances are rather due to multiple scattering effects. The tetrahedral environment of Ga in GaAs displays an intense and narrow main peak at 10376.5 eV with more intense postedge structures due to the higher scattering power of heavier As atoms. On the other hand, the octahedral environment of Ga in α-Ga_2O_3 displays a broader main peak at 10378.5 eV and a postedge feature at 10399 eV. Finally, the mixed environment of Ga in β-Ga_2O_3 exhibits a wider main peak at 10377.5 eV with a shoulder at lower energy than the maximum (10375.5 eV), and a postedge feature at 10397 eV. Thus, β-Ga_2O_3 XANES spectrum can be interpreted as a sum of two spectra corresponding to the octahedral and tetrahedral environments, where the feature at 10377.5 eV cannot be readily resolved. As a result, it is commonly assumed that the broadening of the white line is due to the existence of these two Ga environments. A negative shift is well-known to occur with decreasing

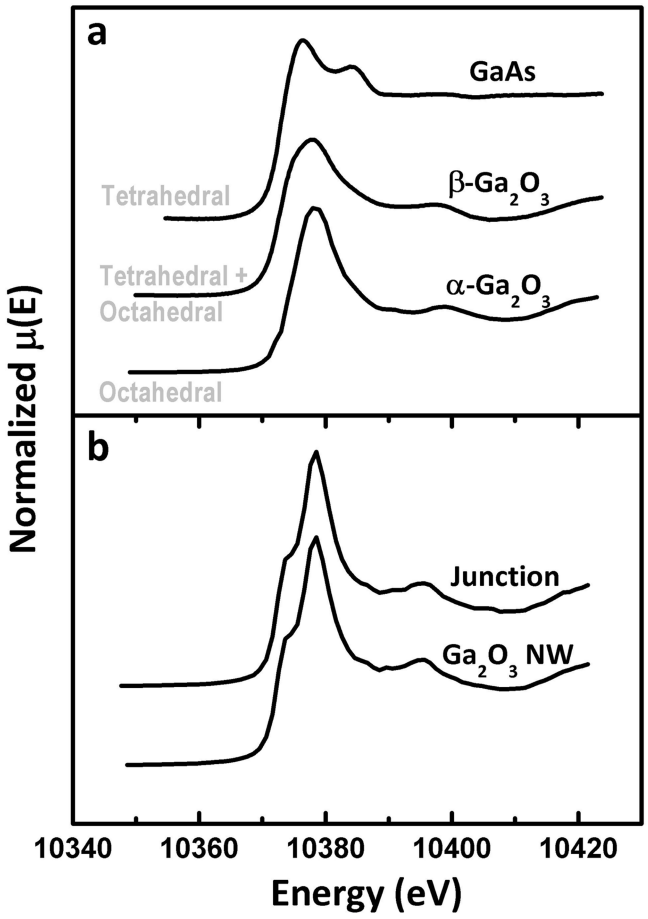

Figure 5. XANES data recorded around the Ga K-edge: (a) Reference materials with tetrahedral (GaAs), tetrahedral + octahedral (β-Ga_2O_3), and octahedral (α-Ga_2O_3) coordination. (b) XANES spectra acquired at the junction and outside a multiwire intersection. The spectra were shifted vertically for clarity.

coordination, and indeed it has been assumed to be an excellent indicator of Ga coordination in the structure.[45]

Figure 5b shows similar XANES spectra acquired inside and outside the nanowire junction. Both spectra show low energy shoulders on the rising limb of the edge that might be explained by contributions from β-Ga_2O_3 and a fairly strong and sharp peak similar to that of α-Ga_2O_3, which contains octahedral Ga sites. The inclusion of α-Ga_2O_3 domains have also been reported in thin films of β-Ga_2O_3 grown by molecular beam epitaxy.[46] Using both α- and β-Ga_2O_3 coordinations, least-squares fits, although not perfect, also points out a mixture of these two environments (see more details in Supporting Information Figure S2). Theoretical XANES spectrum of β-Ga_2O_3 performed by first-principles calculation[47] shows that the rising edge of spectra is mainly composed by tetrahedral site, whereas the strong main peak is composed by octahedral site. In comparison to the β-Ga_2O_3 reference, the intensity ratio between the main peak and shoulder in the collected XANES data is significantly different. In addition, the spectral resonances are better resolved, suggesting that likely a one-dimensional Ga_2O_3 structure has a larger number of multiple-scattering paths than Ga_2O_3 bulk. In general, it has been already reported that the white line intensity is higher and sharper in nanowires than in bulk materials. However, there is no general agreement about the origin of this effect. The phenomenon has

dx.doi.org/10.1021/nl502156h | Nano Lett. XXXX, XXX, XXX−XXX

been associated with an increase of the degree of localization of the p orbitals due to the confinement of the nanowire surfaces,[48] to the larger surface to volume ratio of the nanowires,[49] and to the increase of the attractive electrostatic potential on Ga ions due to the enlargement of its positive effective charge.[50] But our results do not provide extra information to elucidate the origin of this effect and further studies are needed. In principle, the fraction of Ga present as GaO_6 could be estimated from the absorption edge shifts, taking into account that the absorption edge shifts 2 eV in gallium oxides when passing from tetrahedral to octahedral coordination.[45] However, our experimental accuracy of about 1 eV does not allow us to report a convincing fraction from our measurements. In brief, no differences are observed between the spectra taken on the junction and on the wire, suggesting that a major β-Ga_2O_3 phase with α-Ga_2O_3 incorporated in a minor degree dominated all over the multiwire architecture. The crossing point does not induce significant unwanted local structural changes or recrystallization, indicating that a continuous (monolithic) structure has been produced by the self-assembly thermal growth of crossed nanowires. The development of such ordered nanocrosses could start possibly with a self-catalyzed process due to the presence of tin oxide plus pure gallium as source material. At the first stages, Sn atoms could segregate or form tiny droplets at specific points of the Ga_2O_3 wire surface, acting as nucleation centers for the SnO_2 branches. Surface segregation of Sn on the nanowires during growth has been previously found to result in the formation of branched ZnO-based nanostructures.[51] Because the growth temperature is kept constant during the whole process, the quantity of source materials is the key kinetic factor driving the growth of both SnO_2 and Ga_2O_3 oxides.

Recently, it has been reported that Mn-doped Ga_2O_3 takes the spinel structure γ-polymorph in epitaxial films, which is uncommon for undoped bulk material.[52] During the growth of amorphous Ga_2O_3 by means of pulsed laser deposition in a nitrogen-rich atmosphere, it has been also revealed the formation of quasi-binary system $GaN-Ga_2O_3$.[53] Further reports on gallium oxides have also claimed that these gallium oxynitrides, spinel-type compounds, are reaction intermediates during the ammonolysis of various Ga_2O_3 modifications.[54] On the other hand, Ga_2O_3 nanostructures have exhibited a core with crystalline β-Ga_2O_3 phase and an amorphous oxide shell. Moreover, as the particles size decreases, an extended EXAFS analysis also showed that the ratio of the coordination number [Ga(tetrahedral)/Ga(octahedral)] in the β phase decreases and decreases further in the ε phase.[55] In summary, from an experimental point of view Ga_2O_3 compounds range from amorphous to single γ-phase, depending on system dimensionality, size, doping, as well as growth method. Here, according to our XANES results the Ga_2O_3 wires would present a uniform symmetry all over the multiwire architecture that apparently could correspond to a mixture of both α- and β-Ga_2O_3 phases. Thus, a single step growth allows the use for precise control of the local coordination of the nanojunction, providing great flexibility in the structures that can be produced.

In order to get further understanding of the local structure at the wires intersection, EXAFS data were also collected around the Ga K-edge. Figure 6 shows the magnitude of the Fourier transforms (FTs) of the EXAFS functions, as well as EXAFS oscillations accompanied by their best fits in the interval k = 2.7−9.9 $Å^{-1}$ applying a Hanning window. The data quality, though limited to the first few neighbor atom shells, is good if

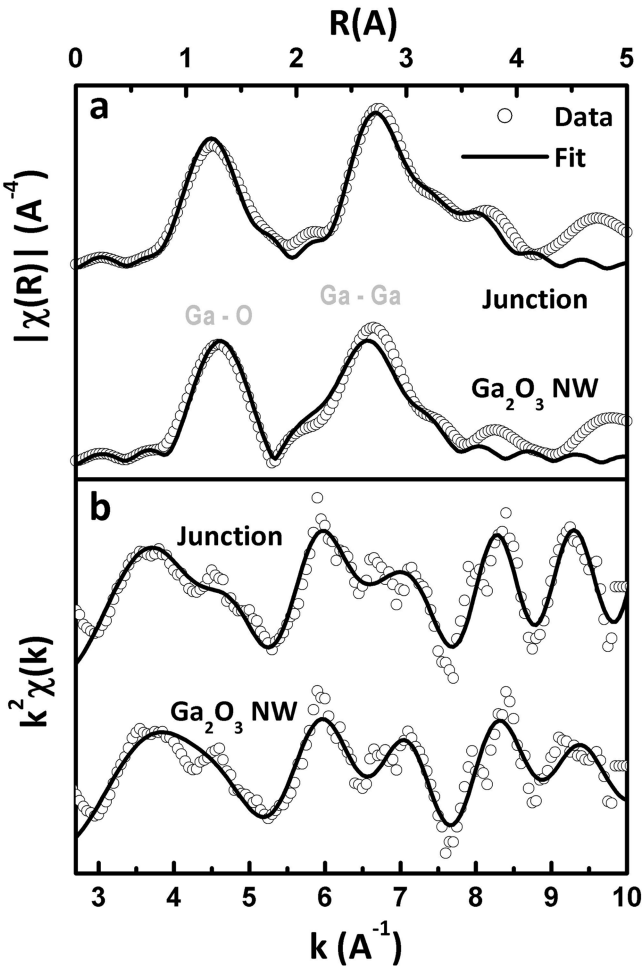

Figure 6. (a) Magnitude of the FTs of the EXAFS functions (open symbols) around the Ga K-edge and their best fits (solid lines) recorded at the junction and outside it. (b) k^2-weight EXAFS oscillations (open symbols) accompanied by their best fits (solid lines) in the interval 2.7−9.9 $Å^{-1}$. For clarity, the spectra were shifted vertically.

we keep into account the difficulties that usually involve an X-ray absorption spectroscopy experiment with an X-ray nanobeam. So far, a major challenge for current X-ray microscopes with submicrometer resolution is to stabilize the focal spot position as a function of energy (monochromator scan) for long periods of time. Using the FEFF code,[56] the EXAFS data analysis was carried out by ab initio modeling of the absorption cross section. Theoretical backscattering amplitudes and phase shifts for all single and multiple scattering paths were calculated using a mixed environment of α-Ga_2O_3 and monoclinic β-Ga_2O_3 model clusters. The α-phase belongs to the $R\bar{3}c$ space group (corundum structure with a = 5.31 Å, and $\alpha = \beta = \gamma = 55.28°$), having a 6-fold octahedral environment with three Ga−O distances of 2.08 Å and three others of 1.92 Å in the GaO_6 octahedra. Thus, in comparison to GaO_4 tetrahedron the two Ga−O distances of the octahedral GaO_6 environment in α-Ga_2O_3 usually decrease the FT magnitude of the EXAFS function. The monoclinic β-phase ($C2/m$ space group structure) with five average coordination number has equally distributed Ga^{3+} ions between octahedral GaO_6 polygons with two averaged distances of 1.95 and 2.06 Å, and distorted tetrahedral GaO_4 units with a mean Ga−O distance of 1.83 Å (lattice parameters a = 12.21 Å, b = 3.04 Å, c

dx.doi.org/10.1021/nl502156h | Nano Lett. XXXX, XXX, XXX−XXX

Table 1. Summary of the Interatomic Distances (R_i), Debye-Waller Factors (σ_i^2) of the First Two Atomic Shells, and the R-Factors Obtained from the Fitting of the FT EXAFS

point	R_{Ga-O} (Å)	$\sigma^2_{Ga-O} \times 10^{-3}$ (Å^2)	R_{Ga-Ga} (Å)	$\sigma^2_{Ga-Ga} \times 10^{-3}$ (Å^2)	R
junction	1.86 ± 0.04	2.8 ± 2.0	3.17 ± 0.03	4.4 ± 1.0	0.02
NW	1.83 ± 0.03	2.3 ± 1.5	3.07 ± 0.02	2.2 ± 1.1	0.04

= 5.80 Å, and β = 103.8°, between a and c). Thus, the two octahedral Ga−O lengths, approximately 0.2 Å longer than tetrahedral Ga−O distances, give rise to bifurcated Ga−O FT peaks in the β-Ga_2O_3 related spectra, decreasing the FT magnitude of the EXAFS functions. In principle, the ratio between the actual and the maximum possible coordination number for each environment could be related to the Ga fraction in GaO_6 and GaO_4. However, because the numbers of oxygen vacancies are unknown, this finding would result in an erroneous estimation.

To compare both EXAFS data collected inside and outside the nanowire junction, the *k*-interval for the Fourier transform has been kept constant from 2.7 to 9.9 Å. The first peak (centered at 1.25 Å) is related to Ga−O distances. The peak magnitude, which is similar inside and outside the nanowire intersection, indicates an ordered environment. The ARTEMIS routine[57] was exploited to fit in *R* space within the window [0−3.4 Å], which included the first and second coordination shells. We have fitted the interatomic distances (R_i) and Debye−Waller (DW) factors (σ_i^2) of the different atomic shells, fixing SO_2 amplitude to 1. The values of the structural parameters extracted from the curve fits (Figure 6b) are reported in Table 1. A fixed coordination of oxygen nearest neighbor atoms and Ga second-nearest-neighbor atoms was applied to both α- and β-Ga_2O_3 polymorphs. The analysis yields 1.83 Å Ga−O distances for the wire, which agrees well with the distance for tetrahedral sites in β-Ga_2O_3 phase. However, for the junction the EXAFS fits yield 1.86 Å Ga−O distance. This finding is comparable to values observed in other compounds with GaO_4 units, like $GaAsO_4$ berlinites (1.83 Å) or $MgGa_2O_4$ spinel (1.89 Å) but is shorter than those with GaO_6 units, such as α-Ga_2O_3 (1.98 Å) or Ga in a rutile phase, Ga/SnO_2 (2.05 Å). Within the experimental error, the second shell supports the results obtained from the first shell. At the crossing point, the Ga shell has larger average interatomic distances (R_{Ga-Ga}) and is more disordered than in the wire (see Debye−Waller factors σ^2_{Ga-Ga}), suggesting that the nanojunction tends to distort and expand locally the Ga_2O_3 lattice. On the other hand, the presence of native defects, which usually involve oxygen vacancies, may lead as well to some deviations from the 1:1 [tetrahedral/octahedral] occupation ratio in β-Ga_2O_3. In fact, according to the EBSD data, the junction region exhibits mixed phases, which could give rise to a core−shell-like structure or an intermediate spinel ($SnGa_2O_4$) phase. Both XANES results and EXAFS analysis confirmed that a mixture of α- and β-Ga_2O_3 sites are involved with six coordination number for the octahedral GaO_6 symmetry of Ga in α-Ga_2O_3 and five average coordination number for the mixed Ga environment in β-Ga_2O_3 composed by half of the Ga atoms in tetrahedral GaO_4 symmetry and the other half in octahedral GaO_6 units. However, these sites are slightly distorted due to the lateral SnO_2 branch in comparison with the well established Ga sites in the above-discussed Ga_2O_3 polymorphs. In addition, our nano-XAS results gave no evidence of large structural defects induced by the Cr incorporation in the Ga_2O_3 host lattice. Although the presence of segregation effects upon doping cannot be completely ruled out, within the sensitivity of our experimental techniques the local Ga environment revealed by X-ray absorption spectroscopy indicates the preservation of a mixed coordination along the wire composed by Ga atoms in tetrahedral GaO_4 sites and in octahedral GaO_6 units, independent of the impurity levels. Moreover, no significant bond length deviations attributed to the dopants were observed. These findings are in good agreement with previous observations, which reported that the presence of Cr in Ga_2O_3 nanowires does not influence strongly in the vibrational properties but only induces in the luminescence an intense red band characteristic of Cr^{3+} in the oxide.[40] In general, our results also highlight the convenience and reliability to obtain uniform dopant distributions in multiwire architectures by a thermal evaporation method.

In summary, we showed the use of a hard X-ray nanoprobe with elemental and local structure specificity to probe the compositional uniformity and symmetry of point contacts between single crossed Cr-doped Ga_2O_3/SnO_2 nanowires grown by thermal evaporation method. Elemental maps displayed Cr, Ga, and Sn atoms homogeneously distributed along the multiwire structure. XANES data around the Ga K-edge showed that there is no significant structural disorder induced by the intersection region. Within the sensitivity of our experimental techniques, XANES spectra exhibited distinguishable peaks that were assigned to the tetrahedral and octahedral Ga sites of β-Ga_2O_3 and α-Ga_2O_3 environments on the basis of a comparison with reference polymorphs. The preliminary EXAFS curve-fitting analysis suggests that likely other phase or defects are present in the crossing point, giving rise to the small changes in the interatomic distances of the first two neighbor shells. Our results support that the self-assembly of crossed multiwires during a single step thermal growth represents a viable strategy for organizing individual nanowires. In principle, the formation mechanisms of interconnected Ga_2O_3/SnO_2 wires could probably be extended to other semiconductor oxide systems.

■ ASSOCIATED CONTENT

Ⓢ Supporting Information

SEM image of a junction of a SnO_2 branch and a Ga_2O_3 wire with a series of nine EBSD patterns, recorded along the line indicated in the SEM image; linear combination of α-Ga_2O_3 and β-Ga_2O_3 performed using ATHENA code. The resulting parameters are R = 0.02; χ^2 = 0.5 and reduced χ^2 = 0.007, while the mixing ratio is about 0.22/0.78 (α-Ga_2O_3/β-Ga_2O_3). This material is available free of charge via the Internet at http://pubs.acs.org.

■ AUTHOR INFORMATION

Corresponding Author

*E-mail: gmartine@esrf.fr.

Notes

The authors declare no competing financial interest.

dx.doi.org/10.1021/nl502156h | *Nano Lett.* XXXX, XXX, XXX−XXX

■ ACKNOWLEDGMENTS

The authors thank Irina Snigireva and Armando Vicente Solé for their assistance with the SEM measurements and data processing using PyMca, respectively. We thank Peter Cloetens and Sylvain Labouré for their help and the ESRF for the beam time allocated. This work has been partially supported by the NANOWIRING Marie Curie ITN (EU project no. PITN-GA-2010-265073) and by MINECO (Projects MAT 2012-31959 and Consolider Ingenio CSD 2009-00013).

■ REFERENCES

(1) Wu, Y.; Xiang, J.; Yang, C.; Lu, W.; Lieber, C. M. *Nature* **2004**, *430*, 61−5.
(2) Huang, Y. *Small* **2005**, *1*, 142−7.
(3) Li, Y.; Qian, F.; Xiang, J.; Lieber, C. M. *Mater. Today* **2006**, *9*, 18−27.
(4) Fuhrer, M. S.; Nygård, J.; Shih, L.; Forero, M.; Yoon, Y.-G.; Mazzoni, M. S. C.; Choi, H. J.; Ihm, J.; Louie, S. G.; Zettl, A.; McEuen, P. L. *Science* **2000**, *288*, 494−7.
(5) Güell, A. G.; Ebejer, N.; Snowden, M. E.; McKelvey, K.; Macpherson, J. V.; Unwin, P. R. *Proc. Natl. Acad. Sci. U.S.A.* **2012**, *109*, 11487−92.
(6) Yoon, H. P.; Maitani, M. M.; Cabarcos, O. M.; Cai, L.; Mayer, T. S.; Allara, D. L. *Nano Lett.* **2010**, *10*, 2897−902.
(7) Ge, J.-P.; Wang, J.; Zhang, H.-X.; Wang, X.; Peng, Q.; Li, Y.-D. *Chem.−Eur. J.* **2005**, *11*, 1889−94.
(8) Rueda-Fonseca, P.; Bellet-Amalric, E.; Vigliaturo, R.; den Hertog, M.; Genuist, Y.; André, R.; Robin, E.; Artioli, A.; Stepanov, P.; Ferrand, D.; Kheng, K.; Tatarenko, S.; Cibert, J. *Nano Lett.* **2014**, *14*, 1877−83.
(9) Zheng, H.; Wang, J.; Huang, J. Y.; Wang, J.; Zhang, Z.; Mao, S. X. *Nano Lett.* **2013**, *13*, 6023−7.
(10) Segura-Ruiz, J.; Martínez-Criado, G.; Denker, C.; Malindretos, J.; Rizzi, A. *Nano Lett.* **2014**, *14*, 1300−5.
(11) Sourribes, M. J. L.; Isakov, I.; Panfilova, M.; Liu, H.; Warburton, P. A. *Nano Lett.* **2014**, *14*, 1643−50.
(12) Pan, D.; Fu, M.; Yu, X.; Wang, X.; Zhu, L.; Nie, S.; Wang, S.; Chen, Q.; Xiong, P.; von Molnár, S.; Zhao, J. *Nano Lett.* **2014**, *14*, 1214−20.
(13) Cheng, G.; Chang, T.-H.; Qin, Q.; Huang, H.; Zhu, Y. *Nano Lett.* **2014**, *14*, 754−8.
(14) Dillen, D. C.; Kim, K.; Liu, E.-S.; Tutuc, E. *Nat. Nanotechnol.* **2014**, *9*, 116−20.
(15) Chou, Y.-C.; Hillerich, K.; Tersoff, J.; Reuter, M. C.; Dick, K. A.; Ross, F. M. *Science* **2014**, *343*, 281−4.
(16) Bussone, G.; Schott, R.; Biermanns, A.; Davydok, A.; Reuter, D.; Carbone, G.; Schülli, TU. .; Wieck, A. D.; Pietsch, U. *J. Appl. Crystallogr.* **2013**, *46*, 887−92.
(17) Yuhas, B. D.; Fakra, S.; Marcus, M. A.; Yang, P. *Nano Lett.* **2007**, *7*, 905−9.
(18) Büsgen, T.; Hilgendorff, M.; Irsen, S.; Wilhelm, F.; Rogalev, A.; Goll, D.; Giersig, M. *J. Phys. Chem. C* **2008**, *112*, 2412−7.
(19) Segura-Ruiz, J.; Martínez-Criado, G.; Chu, M. H.; Geburt, S.; Ronning, C. *Nano Lett.* **2011**, *11*, 5322−6.
(20) López, I.; Utrilla, A. D.; Nogales, E.; Méndez, B.; Piqueras, J.; Peche, A.; Ramírez-Castellanos, J.; González-Calbet, J.-M. *J. Phys. Chem. C* **2012**, *116*, 3935−43.
(21) Díaz, J.; López, I.; Nogales, E.; Méndez, B.; Piqueras, J. J. *Nanopart. Res.* **2011**, *13*, 1833.
(22) Guo, S. *Nanoscale* **2010**, *2*, 2521−9.
(23) Marcu, A.; Yanagida, T.; Nagashima, K.; Oka, K.; Tanaka, H.; Kawai, T. *Appl. Phys. Lett.* **2008**, *92*, 173119.
(24) Nagashima, K.; Yanagida, T.; Oka, K.; Kanai, M.; Klamchuen, A.; Rahong, S.; Meng, G.; Horprathum, M.; Xu, B.; Zhuge, F.; He, Y.; Park, B. H.; Kawai, T. *Nano Lett.* **2012**, *12*, 5684−90.
(25) Dick, K. A.; Deppert, K.; Larsson, M. W.; Mårtensson, T.; Seifert, W.; Wallenberg, L. R.; Samuelson, L. *Nat. Mater.* **2004**, *3*, 380−4.
(26) Gu, Z.; Ye, H.; Bernfeld, A.; Livi, K. J. T.; Gracias, D. H. *Langmuir* **2007**, *23*, 979−82.
(27) Cui, Q.; Gao, F.; Mukherjee, S.; Gu, Z. *Small* **2009**, *5*, 1246−57.
(28) Yao, J.; Yan, H.; Lieber, C. M. *Nat. Nanotechnol.* **2013**, *8*, 329−35.
(29) Garnett, E. C.; Cai, W.; Cha, J. J.; Mahmood, F.; Connor, S. T.; Greyson, C. M.; Cui, Y.; McGehee, M. D.; Brongersma, M. L. *Nat. Mater.* **2012**, *11*, 241−9.
(30) Kang, J.-H.; Cohen, Y.; Ronen, Y.; Heiblum, M.; Buczko, R.; Kacman, P.; Popovitz-Biro, R.; Shtrikman, H. *Nano Lett.* **2013**, *13*, 5190−6.
(31) Plissard, S. R.; van Weperen, I.; Car, D.; Verheijen, M. A.; Immink, G. W. G.; Kammhuber, J.; Cornelissen, L. J.; Szombati, D. B.; Geresdi, A.; Frolov, S. M.; Kouwenhoven, L. P.; Bakkers, E. P. A. M. *Nat. Nanotechnol.* **2013**, *8*, 859−64.
(32) Duan, X.; Huang, Y.; Cui, Y.; Wang, J.; Lieber, C. M. *Nature* **2001**, *409*, 66−9.
(33) Huang, Y.; Duan, X.; Cui, Y.; Lauhon, L. J.; Kim, K.-H.; Lieber, C. M. *Science* **2001**, *294*, 1313−7.
(34) Machon, D.; McMillan, P. F.; Xu, B.; Dong, J. *Phys. Rev. B* **2006**, *73*, 094125.
(35) Nogales, E.; Méndez, B.; Piqueras, J. *Appl. Phys. Lett.* **2005**, *86*, 113112.
(36) Hidalgo, P.; Méndez, B.; Piqueras, J. *Nanotechnology* **2005**, *16*, 2521.
(37) Cebriano, T.; Méndez, B.; Piqueras, J. *J. Nanoparticle Res.* **2013**, *15*, 1−8.
(38) Erwin, S. C.; Zu, L.; Haftel, M. I.; Efros, A. L.; Kennedy, T. A.; Norris, D. J. *Nature* **2005**, *436*, 91−4.
(39) Norris, D. J.; Efros, A. L.; Erwin, S. C. *Science* **2008**, *319*, 1776−9.
(40) López, I.; Nogales, E.; Méndez, B.; Piqueras, J.; Peche, A.; Ramírez-Castellanos, J.; González-Calbet, J.-M. *J. Phys. Chem. C* **2013**, *117*, 3036−45.
(41) López, I.; Nogales, E.; Méndez, B.; Piqueras, J. *Appl. Phys. Lett.* **2012**, *100*, 261910.
(42) Martínez-Criado, G.; Tucoulou, R.; Cloetens, P.; Bleuet, P.; Bohic, S.; Cauzid, J.; Kieffer, I.; Kosior, E.; Labouré, S.; Petitgirard, S.; Rack, A.; Sans, J. A.; Segura-Ruiz, J.; Suhonen, H.; Susini, J.; Villanova, J. *J. Synchrotron Radiat.* **2012**, *19*, 10−8.
(43) Martínez-Criado, G.; Homs, A.; Alén, B.; Sans, J. A.; Segura-Ruiz, J.; Molina-Sánchez, A.; Susini, J.; Yoo, J.; Yi, G.-C. *Nano Lett.* **2012**, *12*, 5829−34.
(44) Solé, V. A.; Papillon, E.; Cotte, M.; Walter, P.; Susini, J. *Spectrochim. Acta, Part B* **2007**, *62*, 63−8.
(45) Charton, P.; Armand, P. *J. Non-Cryst. Solids* **2004**, *333*, 307−15.
(46) Oshima, T.; Okuno, T.; Fujita, S. *Jpn. J. Appl. Phys.* **2007**, *46*, 7217.
(47) Tanaka, I.; Mizoguchi, T.; Matsui, M.; Yoshioka, S.; Adachi, H.; Yamamoto, T.; Okajima, T.; Umesaki, M.; Ching, W. Y.; Inoue, Y.; Mizuno, M.; Araki, H.; Shirai, Y. *Nat. Mater.* **2003**, *2*, 541−5.
(48) Pao, C. W.; Babu, P. D.; Tsai, H. M.; Chiou, J. W.; Ray, S. C.; Yang, S. C.; Chien, F. Z.; Pong, W. F.; Tsai, M.-H.; Hsu, C. W.; Chen, L. C.; Chen, C. C.; Chen, K. H.; Lin, H.-J.; Lee, J. F.; Guo, J. H. *Appl. Phys. Lett.* **2006**, *88*, 223113.
(49) Chiou, J. W.; Kumar, K. P. K.; Jan, J. C.; Tsai, H. M.; Bao, C. W.; Pong, W. F.; Chien, F. Z.; Tsai, M.-H.; Hong, I.-H.; Klauser, R.; Lee, J. F.; Wu, J. J.; Liu, S. C. *Appl. Phys. Lett.* **2004**, *85*, 3220−2.
(50) Chiou, J. W.; Jan, J. C.; Tsai, H. M.; Pong, W. F.; Tsai, M.-H.; Hong, I.-H.; Klauser, R.; Lee, J. F.; Hsu, C. W.; Lin, H. M.; Chen, C. C.; Shen, C. H.; Chen, L. C.; Chen, K. H. *Appl. Phys. Lett.* **2003**, *82*, 3949−51.
(51) Wen, J. G.; Lao, J. Y.; Wang, D. Z.; Kyaw, T. M.; Foo, Y. L.; Ren, Z. F. *Chem. Phys. Lett.* **2003**, *372*, 717−22.
(52) Huang, R.; Hayashi, H.; Oba, F.; Tanaka, I. *J. Appl. Phys.* **2007**, *101*, 063526.
(53) Roehrens, D.; Brendt, J.; Samuelis, D.; Martin, M. *J. Solid State Chem.* **2010**, *183*, 532−41.
(54) Jung, W.-S. *Mater. Lett.* **2006**, *60*, 2954−7.

(55) Zhou, X. T.; Heigl, F.; Ko, J. Y. P.; Murphy, M. W.; Zhou, J. G.; Regier, T.; Blyth, R. I. R.; Sham, T. K. *Phys. Rev. B* **2007**, *75*, 125303.
(56) Ankudinov, A. L.; Ravel, B.; Rehr, J. J. *Phys. Rev. B* **1998**, *58*, 7565−76.
(57) Newville, M. *J. Synchrotron Radiat.* **2001**, *8*, 322−4.

dx.doi.org/10.1021/nl502156h | *Nano Lett.* XXXX, XXX, XXX−XXX